

A new analysis of the WASP-3 system: no evidence for an additional companion

M. Montalto,^{1*} J. Gregorio,² G. Boué,¹ A. Mortier,¹ I. Boisse,¹ M. Oshagh,^{1,3}
M. Maturi,⁴ P. Figueira,¹ S. Sousa¹ and N. C. Santos^{1,3}

¹*Centro de Astrofísica da Universidade do Porto (CAUP), Rua das Estrelas, 4150-762 Porto, Portugal*

²*Atalaia Group, Crow Observatory-Portalegre, 7300 Portalegre, Portugal*

³*Departamento de Física e Astronomia, Faculdade de Ciências, Universidade do Porto, 4169-007 Porto, Portugal*

⁴*Zentrum fuer Astronomie, ITA, Universitaet Heidelberg, Albert-Ueberle-Str. 2, D-69120 Heidelberg, Germany*

Accepted 2012 August 14. Received 2012 July 20; in original form 2012 March 16

ABSTRACT

In this work, we investigate the problem concerning the presence of additional bodies gravitationally bound with the WASP-3 system. We present eight new transits of this planet gathered between 2009 May and 2011 September by using the 30-cm telescope at the Crow Observatory-Portalegre, and analyse all the photometric and radial velocity data published so far. We did not observe significant periodicities in the Fourier spectrum of the observed minus calculated (O – C) transit timing and radial velocity diagrams (the highest peak having false-alarm probabilities of 56 and 31 per cent, respectively) or long-term trends. Combining all the available information, we conclude that the radial velocity and transit timing techniques exclude, at 99 per cent confidence limit, any perturber more massive than $M \gtrsim 100 M_{\text{earth}}$ with periods up to 10 times the period of the inner planet. We also investigate the possible presence of an exomoon in this system and determine that considering the scatter of the O – C transit timing residuals a coplanar exomoon would likely produce detectable transits. This hypothesis is however apparently ruled out by observations conducted by other researchers. In the case where the orbit of the moon is not coplanar, the accuracy of our transit timing and transit duration measurements prevents any significant statement. Interestingly, on the basis of our reanalysis of SOPHIE data we noted that WASP-3 passed from a less active ($\log R'_{\text{HK}} = -4.95$) to a more active ($\log R'_{\text{HK}} = -4.8$) state during the 3 yr monitoring period spanned by the observations. Despite the fact that no clear spot crossing has been reported for this system, this analysis suggests a more intensive monitoring of the activity level of this star in order to understand its impact on photometric and radial velocity measurements.

Key words: techniques: photometric – techniques: radial velocities – planets and satellites: individual: WASP-3b – stars: activity.

1 INTRODUCTION

The field of exoplanets has been blessed in recent years by an impressive flow of new exciting discoveries. As the sample of known exoplanetary systems increases, several interesting characteristics become evident, posing new challenging issues for theories of planet formation and evolution. Given their short periods and large masses, the so-called hot Jupiters were the first class of exoplanets being discovered around solar-type stars (Mayor & Queloz 1995). Those among them later found to transit in front of the disc of the star (Charbonneau et al. 2000) also gained a special importance given

that they allow us to acquire physical information such as the radius and the density of the planet which would remain otherwise inaccessible. At the time of writing this paper, there were 187 known and confirmed transiting planets,¹ and 87 of them had a period smaller than 10 d and a mass larger than $0.7 M_{\text{jup}}$.

Several hypotheses were developed to explain the origin of these objects involving scenarios where these giant planets, while originally forming in remote regions of the planetary system, were then moved to their actual position by means of different possible mechanisms which can be essentially grouped in three broad classes: (i) planet–protoplanetary disc interactions leading to

*E-mail: marco.montalto@astro.up.pt

¹ <http://exoplanets.org/table> (accessed on 2012 March 9).

inward migration of the giant planet (Goldreich & Tremaine 1980; Nelson et al. 2000); (ii) planet–planet scattering in multiplanetary systems (Weidenschilling & Marzari 1996; Chatterjee et al. 2008; Jurić & Tremaine 2008); (iii) Kozai-induced migration in inclined planetary or binary stellar systems (Kozai 1962; Wu & Murray 2003; Fabrycky & Tremaine 2007). While the first class of mechanisms would produce in principle a smooth migration leading to circularized orbits preserving the original alignment between the spin axis of the star and the orbital angular momentum axis of the planet, the other two processes may result in final eccentric orbits and largely misaligned spin–orbit angles. As evidenced by exploiting the Rossiter–McLaughlin (RM) effect (Rossiter 1924; McLaughlin 1924), most transiting exoplanets have spin–orbit angles perfectly consistent with zero, but some of them present surprisingly large misaligned angles (Triaud et al. 2010). These differences highlight the fact that probably all these processes play a role in shaping the structure of these systems (Nagasawa, Ida & Bessho 2008).

To further clarify the relative importance of these different theoretical scenarios and understand in which situations one mechanism may prevail over the others, some additional and important related questions need to be carefully examined. One of them concerns the need to understand if these objects are actually isolated or if other planets or even stellar companions are gravitationally bound with the system. Despite the importance of this topic in the framework of our understanding of hot-Jupiter planets, our knowledge is still far from being complete.

In this paper, while attempting to shed new light on this problem, we considered the case of the transiting hot Jupiter WASP-3b, collecting all the photometric and radial velocity data acquired so far as well as presenting our new photometric measurements. We used this data base to investigate the presence of an additional companion in this system.

WASP-3b is a hot-Jupiter planet with a mass of $2.00 \pm 0.09 M_{\text{Jup}}$ revolving around a main-sequence star of spectral type F7–8V with a period of ~ 1.8 d. Its discovery was announced in 2008 by the WASP Consortium (Pollacco et al. 2008) as a result of a photometric campaign conducted with the robotically controlled WASP-North Observatory located in La Palma and subsequent radial velocity follow-up obtained with the SOPHIE spectrograph at the Observatory de Haute-Provence. The first photometry of WASP-3b was presented in the discovery paper of Pollacco et al. (2008) which used SuperWASP-N together with IAC 80-cm and Keele 80-cm telescope data to refine the properties of the transiting object. Two additional transits of WASP-3b were observed by Gibson et al. (2008) with the RISE instrument mounted on the fully robotic 2-m Liverpool Telescope. Tripathi, Winn & Johnson (2010) observed six transits of WASP-3b at the 1.2-m FLOW telescope and at the 2.2-m University of Hawaii Telescope. Joining their results with those of Pollacco et al. (2008) and Gibson et al. (2008), they concluded that a linear fit to the observed ephemerides was not satisfactory, and that either the errors were underestimated or there was a genuine period variation. Maciejewski et al. (2010) presented six new transits gathered at two 1-m class telescopes (Jena and Rozhen), pointing out that a periodic signal was present in the observed minus calculated (hereafter O – C) transit timing diagram, and that an outer perturbing planet in the system could have best explained the observations. Later on, Christiansen et al. (2011) discussed eight new transits of WASP-3b observed during the NASA *EPOXI* Mission of Opportunity. Despite the high precision of their transit timing measurements, these data have never been used so far to analyse transit timing variations of WASP-3b. Recently, Littlefield (2011) reported five additional transit measurements of WASP-3b which

were observed with the 11-inch Schmidt–Cassegrain Telescope at Jordan Hall in the University of Notre Dame Campus. Despite the larger uncertainties with respect to previous studies, the analysis of Littlefield apparently provided an initial modest support to the hypothesis of Maciejewski et al. (2010). Very recently, Sada et al. (2012) obtained three additional light curves of WASP-3b observing with the KPNO visitor centre 0.5-m telescope and one with the 2.1-m KPNO telescope.

Here we present a study of eight new homogeneously observed transits of WASP-3b. This paper is structured as follows. In Section 2, we present our observations of WASP-3b. In Section 3, we describe the reduction process. In Section 4, we derive the stellar parameters of the host star. In Section 5, we describe our analysis of the photometric data. In Section 6, we present the radial velocity data. In Section 7, we describe our analysis of the radial velocity data. In Section 8, we discuss the O – C transit timing diagram, while in Section 9 we discuss the O – C radial velocity diagram. In Section 10, we discuss our results. Finally, in Section 11, we summarize our results and conclude.

2 OBSERVATIONS

The data described here were acquired at the Crow Observatory-Portalegre in Portugal. Eight different transits of WASP-3b were observed as documented in Table 1. The telescope is a 30-cm aperture Meade LX200 F10, reduced at F5.56 (1668 mm) focal length yielding a total field of view of $\sim 28 \times 19$ arcmin². The images were acquired with a SBIG ST8XME camera whose technical characteristics are reported in Table 2. The pixel scale is 1.1 arcsec pixel^{−1}.

Table 1. Information on our observing runs.

Date	Epoch	T_{exp}	Airmass range	No. of images
15/05/2009	196	90	2.016–1.002	178
13/04/2011	574	90	1.873–1.004	104
26/04/2011	581	90	2.055–1.005	123
02/06/2011	601	150	1.532–1.024	96
20/07/2011	627	150	1.029–2.019	98
13/08/2011	640	150	1.032–1.635	77
26/08/2011	647	150	1.002–1.644	77
08/09/2011	654	150	1.002–1.333	61

Table 2. Technical specifications of the acquisition camera.

Camera SBIG ST8XME specifications	
CCD	Kodak KAF-1603ME + TI TC-237
Pixel array	1530 × 1020 pixel
CCD size	13.8 × 9.2 mm
Total pixels	1.6 million
Pixel size	9 μm × 9 μm
Full well capacity	~100 000 e [−]
Dark current	1 e [−] pixel ^{−1} s ^{−1} at 0 °C
Read-out specifications	
Shutter	Electromechanical
Exposure	0.12–3600 s
Resolution	10 ms
A/D converter	16 bits
A/D gain	2.17 e [−] ADU ^{−1}
Read noise	15 e [−] rms
Binning modes	1 × 1, 2 × 2, 3 × 3
Full frame download	~4 s

The exposure time was fixed either to 90 s or to 150 s; the overhead was 4 s due to the full frame download time. A total of 814 images were acquired and analysed. All of them were in the *I*-band filter.

3 DATA REDUCTION

Bias subtraction and flat fielding were performed with our own software in a standard manner. We constructed a master dark image to identify defective pixels in the image and applied a bad pixel correction algorithm which interpolated the values of the bad pixels with those of the surrounding pixels. Then we used DAOPHOT (Stetson 1987) to derive initial aperture photometry and calculate the point spread function (PSF) of our images. ALLSTAR was used to refine magnitude estimates and centroid positions. We then selected our best seeing image as astrometric reference frame. Coordinate transformations among all the other frames and the reference were calculated using DAOMATCH and DAOMASTER. We took the first 10 best seeing images to construct a master high signal-to-noise ratio (S/N) reference frame with MONTAGE2, and a master list of objects. After that centroid positions and magnitudes were further refined using ALLFRAME (Stetson 1994). Finally, we rederived aperture photometry for each source after subtracting the PSF of all the other objects in our images. After some experiments, we decided to set the aperture radius for each frame to 2.3 times the value of the full width at half-maximum of the corresponding PSF.

3.1 Corrected light curves

We then constructed the flux ratios between our target source (WASP-3b) and several other surrounding comparison stars. We used the first 20 brightest stars in our field of view, and calculated a robust weighted average of their fluxes after removing any linear differential extinction trend as measured in the out-of-transit segments of the light curves. Since the telescope has a German mount, once it crosses the meridian it flips around the field of view of 180°. Once this event happened, we found that it was necessary to apply two distinct normalizations before and after the meridian crossing in order to match the photometric zero-points.

3.2 Time stamps

We report all the mid-exposure times of our measurements to the Barycentric Julian Date (BJD) reference frame and barycentric dynamical time standard (TDB) using the online converter provided by Jason Eastman² (Eastman, Siverd & Gaudi 2010).

4 STELLAR PARAMETERS

We used a combined spectrum of WASP-3 to derive spectroscopic stellar atmospheric parameters, including its effective temperature and metallicity. The spectrum used is a stack of eight individual spectra obtained between 2007 July and August (Pollacco et al. 2008). The spectra were downloaded from the OHP-SOPHIE archive. All spectra were obtained in the HE mode ($R \sim 40\,000$) placing the fibre B on the sky. We used the spectrum in fibre B to subtract any contamination light in fibre A (pointing to WASP-3), after correcting for the relative efficiency of the two fibres. The final spectrum has an S/N of the order of 100 in the 6500 Å region.

We used the methodology and line list described in Santos, Israelian & Mayor (2004). In brief, after the measurement of the line

equivalent widths (EWs), the parameters are obtained making use of a line list of 22 Fe I and nine Fe II lines and forcing both excitation and ionization equilibriums. We refer to Santos et al. for details. The analysis was done in LTE using a grid of Kurucz (1993) model atmospheres and a recent version of the radiative transfer code MOOG (Snedden 1973). The EWs were derived manually using the IRAF *slot* task.

The final obtained stellar parameters are as follows: $T_{\text{eff}} = 6448 \pm 123$ K, $\log g = 4.49 \pm 0.08$ dex, $\xi_t = 2.01 \pm 0.40$ km s⁻¹ and $[\text{Fe}/\text{H}] = -0.02 \pm 0.08$ dex. As a double check, we also independently derived the effective temperature of the star using the line-ratio procedure described in Sousa et al. (2010). This procedure uses a different line list, and the EWs are measured automatically using ARES (Sousa et al. 2007). The effective temperature derived using this method is 6432 ± 94 K, in perfect agreement with the value mentioned above. These values are in agreement with the ones presented in the planet announcement paper (Pollacco et al. 2008), which derived a temperature of 6400 ± 100 K, a surface gravity of 4.25 ± 0.05 dex and a metallicity of 0.00 ± 0.20 dex.

5 TRANSIT ANALYSIS

We modelled the observed transits considering the analytical formula of Mandel & Agol (2002). We adopted, in particular, the following parametrization for the planetary distance to the stellar centre normalized to the stellar radius (z):

$$z^2(t) = \left(\frac{8\pi^2 G}{3P} \right)^{2/3} \rho_*^{2/3} \left[(t - T_0)^2 - \left(\frac{T_d}{2} \right)^2 \right] + (1 + r)^2, \quad (1)$$

where G is the gravitational constant, P is the orbital period of the planet, ρ_* is the mean stellar density, T_0 is the time of transit minimum, T_d is the total transit duration (from the first to the fourth contact) and r is the ratio of the planetary radius to the stellar radius. We fit each light curve with the Levenberg–Marquardt algorithm (Press et al. 1992). We made use of the partial derivatives of the flux loss calculated by Pál (2008) as a function of the radius ratio r and the normalized distance z .

The flux F of the star at each given instant of time t during the transit (corresponding to the normalized distance z) was assumed to be

$$F(z(t)) = F_{\text{MA}}(z(t)) + A \times \text{Air}(t) + B, \quad (2)$$

where F_{MA} is the flux loss predicted by the Mandel & Agol (2002) formula, $\text{Air}(t)$ is the airmass at instant t , and A and B are two parameters to account for a residual photometric trend with airmass and a constant zero-point offset. We therefore assumed six free parameters: the time of transit minimum (T_0), the airmass coefficient (A), the constant zero-point B , the planet to star radius ratio (r), the transit duration (T_d) and the mean stellar density (ρ_*). We assumed a quadratic limb-darkening law whose coefficients were fixed interpolating the tables of Claret & Bloemen (2011) in correspondence to the spectroscopic parameters of the star. This procedure yielded the following coefficients in the *I* band: $g_1 = 0.2150$ for the linear term and $g_2 = 0.3034$ for the quadratic term. The orbital period of the planet was fixed as well at the value of $P = 1.846\,834$ d (Pollacco et al. 2008). For each iteration, the Levenberg–Marquardt algorithm calculated the reduced χ_{red} of the fit defined as

$$\chi_{\text{red}} = \sqrt{\frac{\sum_{i=1}^{i=N} (O_i - F_i)^2}{N - N_{\text{free}}}}, \quad (3)$$

² <http://astroutils.astronomy.ohio-state.edu/time/utc2bjd.html>

where O_i is the observed flux corresponding to the i th measurement, F_i is the model-calculated flux as described above, N is the total number of measurements and N_{free} is the number of free parameters. The Levenberg–Marquardt algorithm found the best solution by means of χ_{red} minimization. This solution is however only a formal solution; the best parameters and their uncertainties were then found using a Markov chain algorithm as described below.

5.1 Uncertainties of the observations

To each measurement in our data sets, we associated an uncertainty accordingly to the photon noise and the read-out noise as determined by DAOPHOT. These errors were then added in quadrature to the scatter of the residual fluxes of the comparison stars around our derived mean averaged values (see Section 3.1), and then rescaled in such a way that the best models we fit to the data produced a $\chi^2 = 1$. As pointed out by Pont, Zucker & Queloz (2006), the presence of correlated noise in the data strongly limits the precision of the observations. The uncertainties calculated by DAOPHOT already accounted for some obvious noise correlations. This is evident in Fig. 1 where we plot the uncertainty of the measurements as a function of airmass and seeing. This ensured that the transits are fitted giving more weight to those measurements acquired under the best observing conditions. Nonetheless, it may well be that the noise in our data is correlated also with some other non-trivial variables that our reduction did not take into account. In order to verify this hypothesis, we created some mock light curves of our model-subtracted light curves assuming that each simulated point was distributed normally around zero but with a time-dependent dispersion equal to the uncertainty of the corresponding real data. We then compared the rms of the real and simulated light curves averaged over time-scales between 10 and 30 min. The average ratio of the dispersions of the real to the simulated data (σ_r/σ_s) was always smaller than 1, with the exception of epoch 574 ($\sigma_r/\sigma_s = 1.09$) and epoch 627 ($\sigma_r/\sigma_s = 1.04$) observations. For these two nights we expanded our uncertainties by these factors, whereas for the remaining nights we did not apply any other correction.

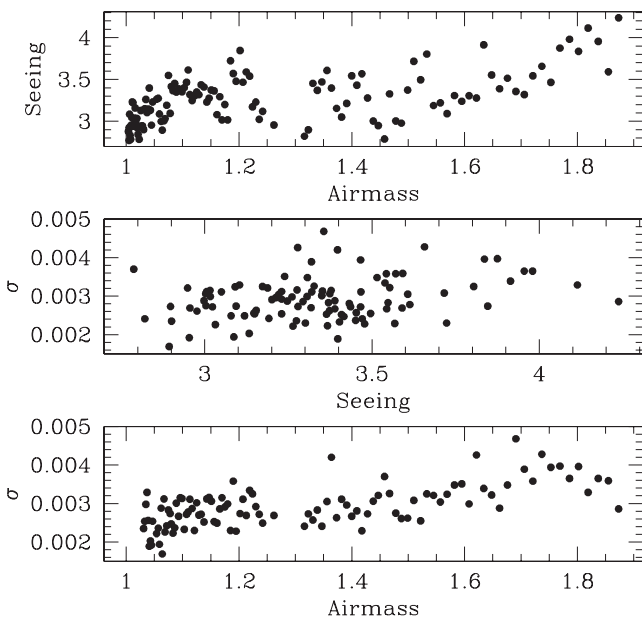


Figure 1. Noise correlation with atmospheric indicators relative to 2011 April 13.

5.2 Markov chain Monte Carlo analysis

A commonly used approach to derive parameter uncertainties in the exoplanetary literature (e.g. Gazak et al. 2012) is based on Markov chain Monte Carlo analysis. We implemented our own version of the Markov chain algorithm along the following lines. For each transit light curve we created five chains of 10^5 steps. Each chain is started from a point 5σ away (in one randomly selected free parameter) from the best-fitting solution obtained by the Levenberg–Marquardt algorithm, where the σ values of the parameters considered are those that are obtained by the same transit fitting algorithm as described in Section 5. The χ_{old}^2 of the fit of this initial solution is recorded and compared with the χ_{new}^2 obtained in the following step. The following step is obtained by jumping from the initial position to another one in the multidimensional parameter space randomly selecting one of the free parameters and changing its value by an arbitrary amount which is dependent on a jump constant and the uncertainty σ of the parameter itself. Steps are accepted or rejected according to the Metropolis–Hastings criterion. If χ_{new}^2 is lower than χ_{old}^2 the step is executed, otherwise the execution probability is $P = e^{-\Delta\chi^2/2}$, where $\Delta\chi^2 = \chi_{\text{new}}^2 - \chi_{\text{old}}^2$. In this latter situation, a random number between 0 and 1 is drawn from a uniform probability distribution. If this number is lower than P then the step is executed, otherwise the step is rejected and the previous step is repeated instead in the chain. In any case, the value of the χ^2 of the last step is recorded and compared with the one of the following step up to the end of the chain. We adjusted the jump constants (one for each parameter) in such a way that the step acceptance rate for all the parameters was around 25 per cent. The convergence among the five separate chains was checked by comparing the variances within and between the different chains by means of the Gelman & Rubin (1992) statistic. In all cases, the value of the Gelman–Rubin statistic was within a few per cent from unity, indicating that the chains were converged and well mixed. We then excluded the first 20 per cent of steps of each chain to avoid the initial burn-in phase, and for each parameter we merged the remaining part of the chains together. Then we derived the mode of the resulting distributions, and the 68.3 per cent confidence limits defined by the 15.85th and the 84.15th percentiles in the cumulative distributions.

We ran two separate groups of chains by first considering as free parameters T_0 , A and B while retaining the others fixed at the best values obtained by the Levenberg–Marquardt algorithm. In the second step, we instead perturbed ρ_* , T_d and r while retaining the remaining parameters fixed at the values obtained in the first step. Perturbing all the parameters together leads in general to unstable convergence in particular for the airmass and zero-point coefficients, so we decided to split the procedure into two steps. Fig. 2 shows our observed transits together with our best-fitting models and residuals.

5.3 Mean stellar density

The mean stellar density is one of the most important parameters that can be extracted from transiting planet light curves (Sozzetti et al. 2007). It is interesting to compare the stellar density derived from the analysis of our light curves to the value obtained from the analysis of other data sets.

We then considered the precise transit light curve of WASP-3b obtained by Tripathi et al. (2010) in the Sloan z' -band filter with the University of Hawaii 2.2-m telescope. We chose this transit because all the other transits of WASP-3b published so far (both by Tripathi and by other authors) have been observed with smaller

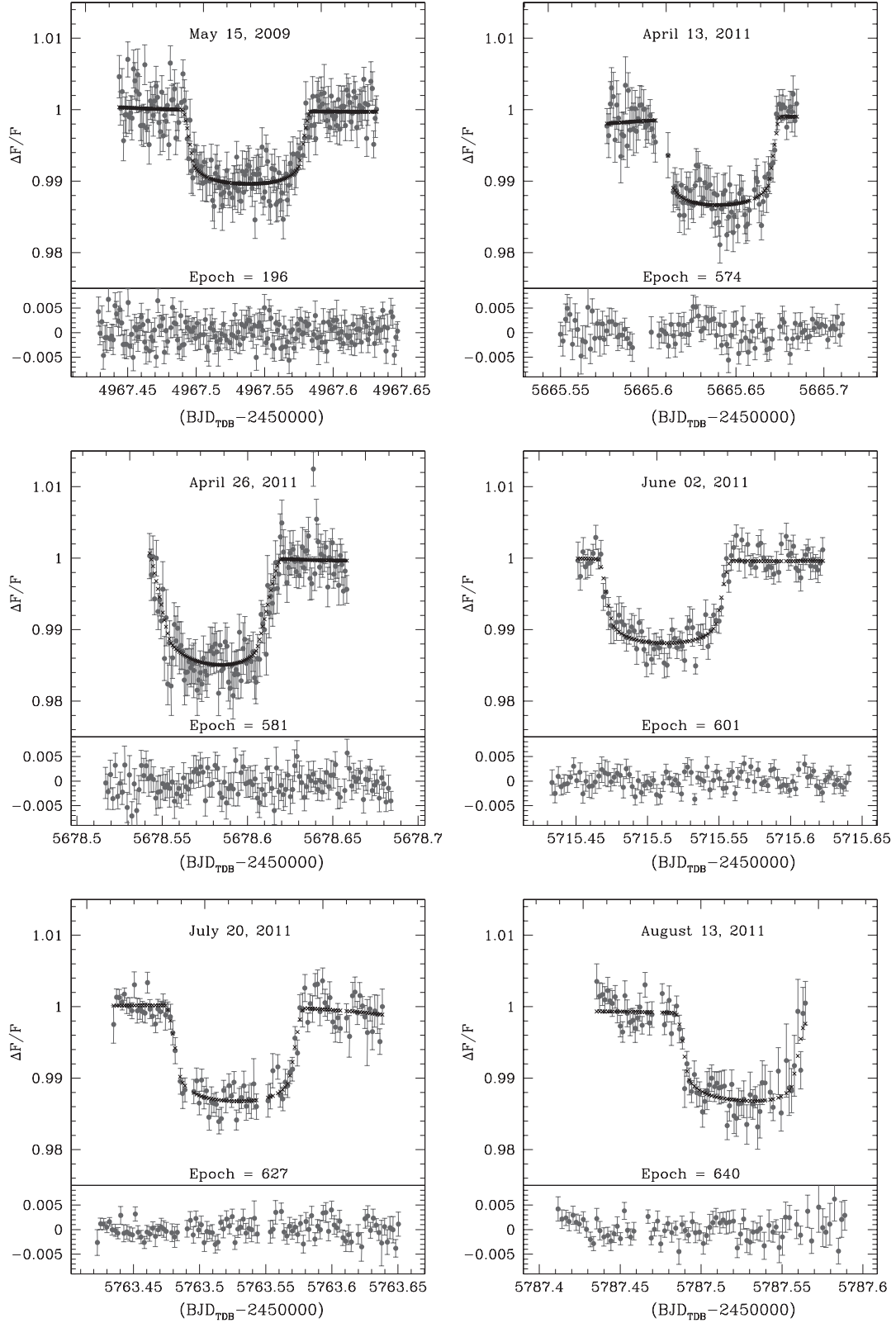


Figure 2. Observed transits of WASP-3b along with our best-fitting models and residuals.

telescopes, and because, the observations being carried out in a near-infrared filter, the impact of limb darkening on the transit shape should be lower than at shorter wavelengths. We performed on this light curve the fit and the statistical analysis previously described,

obtaining final values for the parameters consistent with those of Tripathi et al. (2010). For the mean stellar density, we obtained $\rho_* = 0.50^{+0.15}_{-0.06} \text{ g cm}^{-3}$. In contrast, the analysis of our light curves favours a larger density of $\rho_* = 0.80 \pm 0.07 \text{ g cm}^{-3}$ by taking the

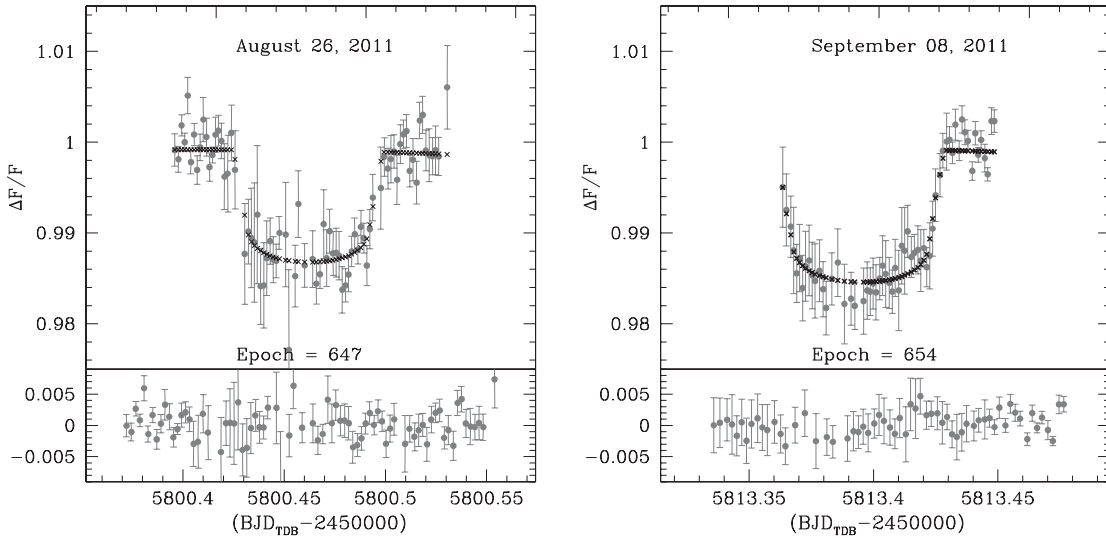


Figure 2 – continued

mean average of the results reported in Table 3. We note that while these estimates are consistent within 2σ , the value obtained from our light curves is more similar to the one reported by Pollacco et al. (2008), $\rho_\star = 0.55^{+0.15}_{-0.05} \rho_\odot = 0.77^{+0.21}_{-0.07} \text{ g cm}^{-3}$, and Miller et al. (2010), $\rho_\star = 0.67^{+0.05}_{-0.06} \rho_\odot = 0.94^{+0.07}_{-0.08} \text{ g cm}^{-3}$.

5.4 Results

In Table 3, we reported for each transit our measured transit durations (T_d) and planet to stellar radius ratios (r). In particular, we observed a weighted average transit duration T_d of 158 ± 1 min, which is closer to the value reported by Pollacco et al. (2008), $T_d = 159.8^{+1.3}_{-2.6}$ min, and Maciejewski et al. (2010), $T_d = 161.2 \pm 2.3$ min, than those reported by Tripathi et al. (2010), $T_d = 168.8 \pm 0.7$ min, and Gibson et al. (2008), $T_d = 165.2^{+1.2}_{-0.8}$ min.

Our weighted average planet to stellar radius ratio (r) is 0.1061 ± 0.0007 and it is consistent with the value reported by Maciejewski et al. (2010), $r = 0.108 \pm 0.003$, and Tripathi et al. (2010) for the z' filter, $r = 0.1099^{+0.0006}_{-0.0010}$, but it is larger than the values given by Pollacco et al. (2008), $r = 0.1030^{+0.0010}_{-0.0015}$, and Gibson et al. (2010), $r = 0.1014^{+0.0010}_{-0.0008}$.

Table 4 lists the collection of transit timings of WASP-3b presented in published papers, along with our new measurements. Our timing errors lie between 80 and 233 s. Note that Maciejewski et al. (2010) transit timings are expressed in BJD based on Terrestrial Time (TT). The difference with respect to BJD based on TDB is however negligible for our purposes (Eastman et al. 2010). Transit timings of Pollacco et al. (2008), Tripathi et al. (2010) and Gibson et al. (2010) have been corrected to account for the conversion between HJD and BJD_{TDB}.³

We considered all the transit ephemerides presented in Table 4 and recalculated the transit period by fitting a weighted linear least-squares model to all the data obtaining

$$T_C(E) = (245\,4605.5601 \pm 0.0002) + E \times (1.846\,834 \pm 0.000\,001), \quad (4)$$

where E is the transit epoch. We then subtracted the model from the observed ephemerides which gave the ($O - C$) residuals presented

in Table 4 and Fig. 3. Our measurements are consistent with the calculated ephemerides with the exception of those relative to epochs 196 and 574. The reduced chi-squared value of the fit ($\sqrt{\chi_r^2}$) is equal to 2.30, obtained from all the 40 measurements reported in Table 4 and considering two degrees of freedom.

In order to further check our measurements of ephemerides, we applied the barycentric method (Szabó et al. 2006; Oshagh et al. 2012). This technique calculates the transit centre (T_C) as the flux weighted average epoch across the transit:

$$T_C = \frac{\sum_{i=1}^{i=N} t_i(1 - f_i)}{\sum_{i=1}^{i=N} (1 - f_i)}, \quad (5)$$

where f_i is the normalized flux, t_i is the time and N is the total number of measurements within one transit. The transit fitting and barycentric method results agree within 1.9σ (where σ is the average of the uncertainties reported in Table 4) for all the transits with the exception of the transit occurring at epoch 640 (3.7σ). In any case, we note that this transit is almost a partial transit which is at the limit of applicability of the barycentric method.

6 RADIAL VELOCITIES

Radial velocities can be used together with transit timing variations to place more stringent constraints on the presence of a perturbing object in the WASP-3b system. We therefore gathered all the radial velocity measurements of WASP-3b publicly available from the Exoplanet Orbit data base.⁴ These measurements were presented in Pollacco et al. (2008), Simpson et al. (2010) and Tripathi et al. (2010), and in the following we first introduce these data sets in more detail.

6.1 Available data sets

Pollacco et al. (2008) obtained seven radial velocity measurements of WASP-3 using the SOPHIE spectrograph at the 1.93-m telescope at Haute-Provence Observatory. The observations were performed between 2007 July 2–5 and August 27–30. All the measurements were acquired outside the transit. Simpson et al. (2010) acquired 26 spectra of WASP-3 during the transit occurring on the night of

³ Jason Eastman's BJD Converter, <http://astroutils.astronomy.ohio-state.edu/time/>.

⁴ <http://exoplanets.org/>

Table 3. Best-fitting transit parameters.

Date	Epoch (E)	Slope (s)	Constant (c)	R_p/R_s (r)	Duration (T_d) (min)	Mean stellar density (ρ_*) (g cm^{-3})
15/05/2009	196	$0.00060^{+0.00074}_{-0.00060}$	$0.99913^{+0.00077}_{-0.00094}$	$0.09506^{+0.00309}_{-0.00123}$	$156.4^{+4.7}_{-2.3}$	$1.05740^{+0.02047}_{-0.42994}$
13/04/2011	574	$-0.00164^{+0.00115}_{-0.00172}$	$1.00068^{+0.00203}_{-0.00135}$	$0.10383^{+0.00256}_{-0.00110}$	$145.4^{+3.2}_{-2.6}$	$1.37746^{+0.02257}_{-0.45132}$
26/04/2011	581	$0.00393^{+0.00115}_{-0.00268}$	$0.99571^{+0.00225}_{-0.00225}$	$0.12177^{+0.00172}_{-0.00319}$	$166.0^{+5.0}_{-5.0}$	$0.51945^{+0.25213}_{-0.06303}$
02/06/2011	601	$0.00078^{+0.00123}_{-0.00185}$	$0.99882^{+0.00187}_{-0.00153}$	$0.10226^{+0.00269}_{-0.00134}$	$162.1^{+5.0}_{-2.5}$	$0.80799^{+0.16908}_{-0.24422}$
20/07/2011	627	$-0.00223^{+0.00106}_{-0.00106}$	$1.00243^{+0.00095}_{-0.00142}$	$0.10904^{+0.00128}_{-0.00192}$	$168.1^{+3.8}_{-2.3}$	$0.82458^{+0.09406}_{-0.20157}$
13/08/2011	640	$-0.00274^{+0.00163}_{-0.00163}$	$1.00208^{+0.00149}_{-0.00223}$	$0.10222^{+0.00249}_{-0.00166}$	$157.8^{+5.1}_{-2.0}$	$1.01379^{+0.03735}_{-0.35486}$
26/08/2011	647	$-0.00080^{+0.00150}_{-0.00137}$	$0.99998^{+0.00143}_{-0.00175}$	$0.10534^{+0.00267}_{-0.00293}$	$147.0^{+10.4}_{-4.2}$	$1.09265^{+0.22601}_{-0.48430}$
08/09/2011	654	$-0.00122^{+0.00205}_{-0.00308}$	$1.00056^{+0.00312}_{-0.00312}$	$0.11422^{+0.00304}_{-0.00203}$	$163.8^{+5.4}_{-3.3}$	$0.95100^{+0.05262}_{-0.31570}$

Table 4. Collection of transit timing measurements of WASP-3b in chronological order.

Epoch	Time of transit minimum (BJD _{TDB} – 245 0000)	$\Delta^-(\text{BJD}_{\text{TDB}})$ (d)	$\Delta^+(\text{BJD}_{\text{TDB}})$ (d)	(O – C) (s)	$\Delta^-(\text{O} - \text{C})$ (s)	$\Delta^+(\text{O} - \text{C})$ (s)	Reference
–250.0	4143.851 04	0.000 40	0.000 40	–46.0	35.0	35.0	Pollacco et al. (2008)
–2.0	4601.865 88	0.000 27	0.000 27	–44.0	23.0	23.0	Tripathi et al. (2010)
0.0	4605.560 30	0.000 35	0.000 35	21.0	30.0	30.0	Gibson et al. (2008)
12.0	4627.721 72	0.000 31	0.000 31	–30.0	27.0	27.0	Tripathi et al. (2010)
18.0	4638.804 03	0.000 31	0.000 31	83.0	27.0	27.0	Tripathi et al. (2010)
30.0	4660.965 09	0.000 21	0.000 21	1.0	18.0	18.0	Tripathi et al. (2010)
40.0	4679.432 69	0.000 50	0.000 50	–63.0	43.0	43.0	Christiansen et. al. (2011)
41.0	4681.279 11	0.000 40	0.000 40	–99.0	35.0	35.0	Christiansen et. al. (2011)
42.0	4683.127 40	0.000 35	0.000 35	27.0	30.0	30.0	Christiansen et. al. (2011)
43.0	4684.974 86	0.000 27	0.000 27	81.0	23.0	23.0	Christiansen et. al. (2011)
44.0	4686.820 53	0.000 59	0.000 59	–19.0	51.0	51.0	Christiansen et. al. (2011)
46.0	4690.513 81	0.000 55	0.000 55	–53.0	48.0	48.0	Christiansen et. al. (2011)
47.0	4692.361 17	0.000 43	0.000 43	–7.0	37.0	37.0	Christiansen et. al. (2011)
48.0	4694.207 11	0.000 42	0.000 42	–84.0	36.0	36.0	Christiansen et. al. (2011)
59.0	4714.522 84	0.000 36	0.000 36	–36.0	31.0	31.0	Gibson et al. (2008)
194.0	4963.844 36	0.000 72	0.000 72	–128.0	62.0	62.0	Tripathi et al. (2010)
194.0	4963.845 63	0.000 55	0.000 55	–18.0	48.0	48.0	Sada et al. (2012)
196.0	4967.536 51	0.000 57	0.000 85	–259.0	49.0	73.0	This work
201.0	4976.773 65	0.000 51	0.000 51	–3.0	44.0	44.0	Tripathi et al. (2010)
236.0	5041.412 71	0.000 49	0.000 49	–14.0	42.0	42.0	Maciejewski et al. (2010)
249.0	5065.419 95	0.000 59	0.000 59	–152.0	51.0	51.0	Maciejewski et al. (2010)
256.0	5078.348 73	0.000 58	0.000 58	–71.0	50.0	50.0	Maciejewski et al. (2010)
269.0	5102.359 33	0.000 56	0.000 56	81.0	48.0	48.0	Maciejewski et al. (2010)
289.0	5139.297 13	0.000 49	0.000 49	178.0	42.0	42.0	Maciejewski et al. (2010)
379.0	5305.510 82	0.000 39	0.000 39	60.0	34.0	34.0	Maciejewski et al. (2010)
403.0	5349.834 57	0.000 39	0.000 39	37.0	34.0	34.0	Sada et al. (2012)
403.0	5349.831 82	0.000 39	0.000 39	–200.0	34.0	34.0	Sada et al. (2012)
404.0	5351.683 20	0.001 10	0.001 10	192.0	95.0	95.0	Littlefield (2011)
430.0	5399.699 90	0.001 50	0.001 50	108.0	130.0	130.0	Littlefield (2011)
436.0	5410.780 20	0.001 30	0.001 30	47.0	112.0	112.0	Littlefield (2011)
450.0	5436.635 90	0.000 80	0.000 80	49.0	69.0	69.0	Littlefield (2011)
456.0	5447.715 50	0.000 80	0.000 80	–72.0	69.0	69.0	Littlefield (2011)
574.0	5665.646 27	0.000 69	0.000 56	305.0	60.0	48.0	This work
581.0	5678.570 65	0.001 06	0.000 87	6.0	92.0	75.0	This work
592.0	5698.883 58	0.000 60	0.000 60	–188.0	52.0	52.0	Sada et al. (2012)
601.0	5715.506 08	0.000 74	0.000 60	–102.0	64.0	52.0	This work
627.0	5763.525 52	0.000 70	0.000 47	50.0	60.0	41.0	This work
640.0	5787.533 79	0.000 80	0.000 80	1.0	69.0	69.0	This work
647.0	5800.461 12	0.001 13	0.001 70	–43.0	98.0	147.0	This work
654.0	5813.387 92	0.000 98	0.000 80	–133.0	85.0	69.0	This work

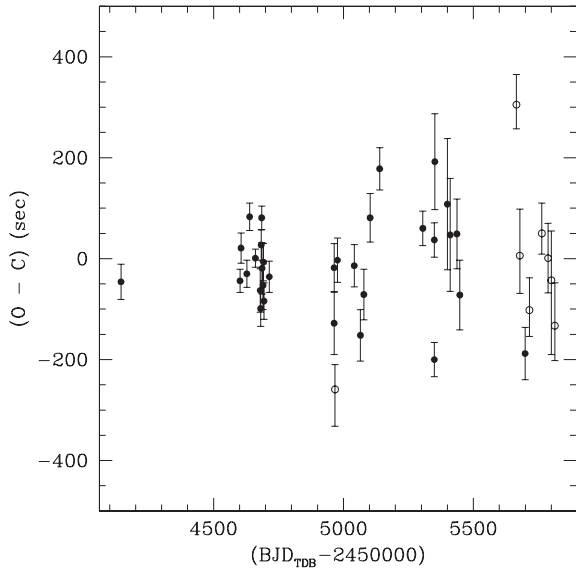


Figure 3. O – C times of transit minimum. Filled circles denote the previous literature results, while open circles denote the new measurements presented in this work.

2008 September 30. The observations were also obtained with the SOPHIE spectrograph at the 1.93-m telescope at Haute-Provence Observatory. These authors also reanalysed the seven measurements presented in Pollacco et al. (2008) based on an updated version of the SOPHIE pipeline. We therefore decided to use these data in our study and not the original data presented in Pollacco et al. (2008).

Tripathi et al. (2010) obtained 33 radial velocity measurements of WASP-3b with the High Resolution Spectrometer (HIRES; Vogt et al. 1994) on the Keck I 10-m telescope at the W. M. Keck Observatory on Mauna Kea. The observations were acquired both during the transit (on 2008 June 19, 21 and 2009 June 3) and outside the transit on several other nights in 2008 and 2009.

7 ANALYSIS OF THE RADIAL VELOCITY DATA

We analysed simultaneously all the radial velocity measurements presented both by Tripathi et al. (2010) and Simpson et al. (2010). Since many measurements were acquired during the transit, we fit the data with a model describing both the Keplerian motion of the host star and the RM anomaly. On the one hand, we modelled the Keplerian motion as

$$RV = \tilde{K} \frac{\cos u + k}{\sqrt{1 - h^2 - k^2}} + \gamma, \quad (6)$$

where \tilde{K} is the radial velocity semiamplitude without the contribution of the eccentricity e , $k = e \cos \omega$, $h = e \sin \omega$, γ is the barycentric radial velocity and $u = \nu + \omega$ is the true argument of latitude with ν the true anomaly and ω the argument of the pericentre.

On the other hand, we accounted for the RM anomaly following Hirano et al. (2010) but including an improved treatment of the RM effect during the partial phases of the transit (as detailed in Appendix B):

$$RV_{RM} = -df \times v_p \left[p - q \left(\frac{v_p}{v \sin i} \right)^2 \right] \quad (7)$$

where df is the flux loss due to the transit of the planet in front of the disc of the star, which we modelled as in Mandel & Agol

Table 5. Adopted values for the p and q parameters and for the limb-darkening coefficients entering in the RM model.

p	q	g_1	g_2	Reference
1.51	0.44	0.596	0.215	Tripathi et al. (2010)
1.72	0.005 46	0.69	0.0	Simpson et al. (2010)

(2002), p and q are two parameters related to modellization of the RM effect as proposed by Hirano et al. (2010) and were fixed to the values adopted by Tripathi et al. (2010) and Simpson et al. (2010) as reported in Table 5, v_p is the average velocity of the star below the area occulted by the planet (Hirano et al. 2010 and Appendix B) and $v \sin i$ is the rotation velocity of the star.

We considered the following free parameters: \tilde{K} , h , k , λ (the spin-orbit angle), $v \sin i$ and γ . Both Tripathi et al. (2010) and Simpson et al. (2010) distinguished two different groups of data in their own data set to account for possible systematic radial velocity variations during their observing runs. We decided to perform the fit twice, first following the analysis of those authors and therefore allowing for a total number of four different barycentric radial velocities. Then, we redid the fit considering only two different barycentric radial velocities for the Tripathi et al. (2010) and Simpson et al. (2010) data sets. This second approach was intended to check for possible long-term variations among the RV residuals that could have been cancelled out by the adoption of a larger number of free parameters. Then, in the end, we considered either nine or seven free parameters for the two fits, respectively. We note that Tripathi et al. (2010) excluded from the fit three data points which were presenting a clearly deviant radial velocity with respect to the remaining measurements. This radial velocity *spike* was ultimately attributed by the authors to residual moonlight unexpectedly leaking into the spectrograph and therefore we neglected them hereafter. Additionally, Tripathi et al. (2010) added in quadrature to the uncertainties of their data a value equal to 14.8 m s^{-1} to account for jitter noise. Since, however, it is not clear which is the origin of this noise, we did not apply this correction.

The convergence towards the best-fitting solution was obtained by means of a Levenberg–Marquardt algorithm, and the uncertainties and the best-fitting values of the parameters by means of a Markov chain Monte Carlo analysis as done for the photometric data. The radial velocity measurements after subtraction of the barycentric velocities, along with the best-fitting model and distinguished in the four (two) different groups of data to which the different γ were applied, are shown in Fig. 4 (upper panels). The result after the subtraction of the RM anomaly is shown in the middle panels of Fig. 4, and the residual velocities after subtracting the Keplerian orbit also are shown in the bottom panels. Our best-fitting parameters are given in Table 6 along with the values obtained by other authors. Our best-fitting model corresponds to $\sqrt{\chi_r^2} = 1.5$ for the 4γ solution and to $\sqrt{\chi_r^2} = 1.6$ for the 2γ solution. Our results are in agreement with the literature values. The barycentric velocities for the case of the 4γ solution are consistent with those derived by Tripathi et al. (2010) and Simpson et al. (2010), and in the case of the 2γ solution our values for each data set are in between the results reported by those authors for their own data. We obtained a value of the spin-orbit angle consistent with zero. We also note that the rotation velocity we obtained for the 4γ solution ($v \sin i = 13.9^{+0.3}_{-0.5}$) is perfectly consistent with the result of Miller et al. (2010) implying $v \sin i = 13.9^{+0.03}_{-0.03}$. For the 2γ solution, we obtained instead a larger value of the rotation velocity ($v \sin i = 14.5^{+0.3}_{-0.3}$).

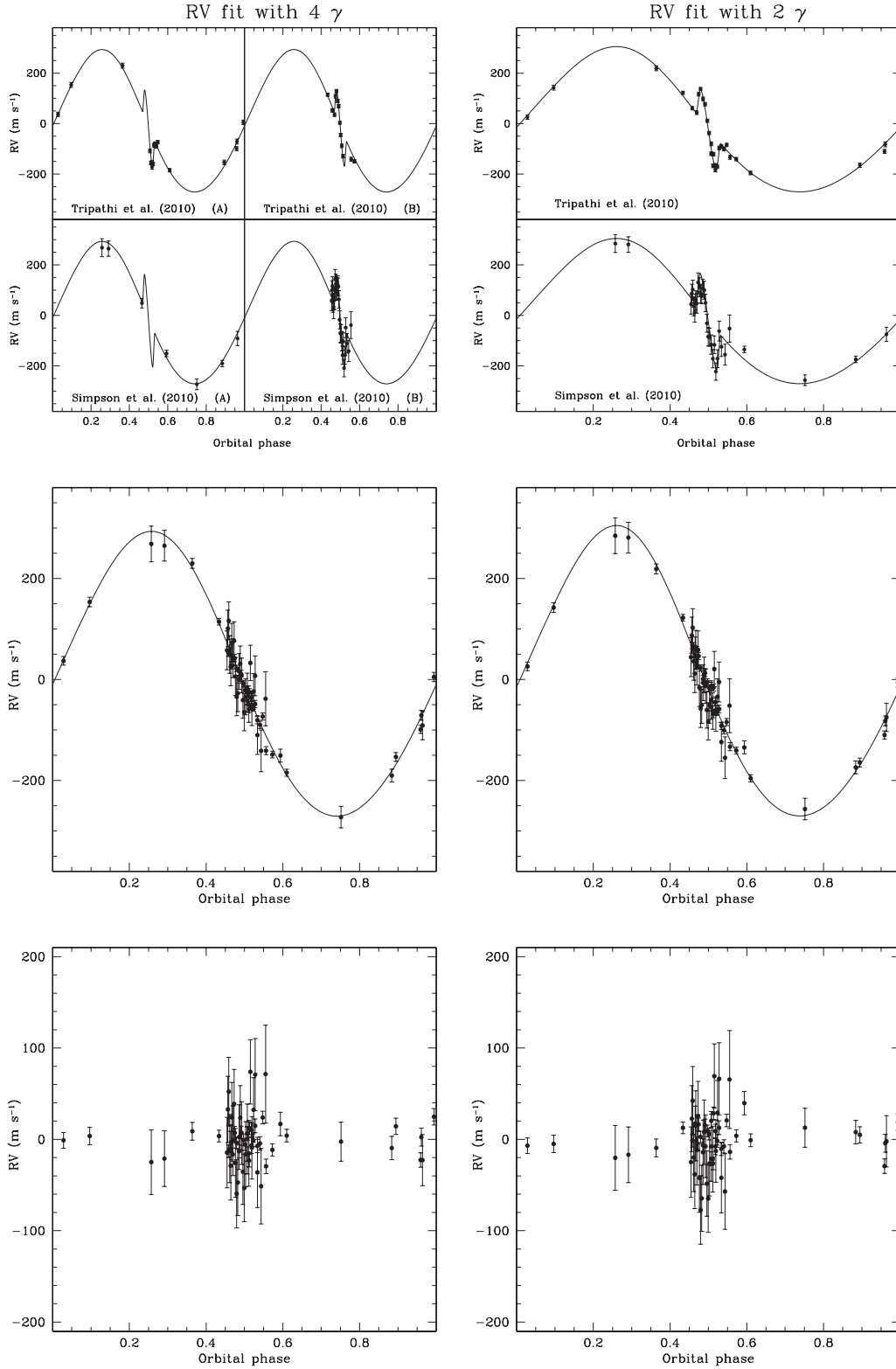


Figure 4. Radial velocity fit considering four and two values of γ as described in the text (left- and right-hand panels, respectively). Top panels: radial velocity measurements along with our best-fitting models. Barycentric radial velocities are subtracted. Middle panels: all radial velocity measurements after subtraction of the barycentric velocities and the RM anomaly. Bottom panels: radial velocity measurements after subtraction of the barycentric velocities, the RM anomaly and the Keplerian orbit.

Table 6. Best-fitting parameters obtained from our reanalysis of the radial velocity measurements (TW: this work), and from the studies of Simpson et al. (2010, SI10), Tripathi et al. (2010, TR10), Miller et al. (2010, MI10) and Pollacco et al. (2008, PO08).

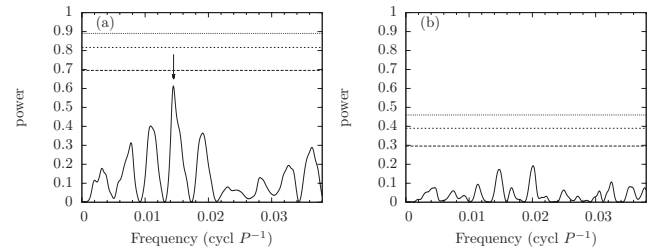
$v \sin i$ (km s ⁻¹)	λ (°)	\tilde{K} (m s ⁻¹)	k	h	γ_1 (km s ⁻¹)	γ_2 (km s ⁻¹)	γ_3 (km s ⁻¹)	γ_4 (km s ⁻¹)	Reference
$13.9^{+0.3}_{-0.5}$	-3^{+1}_{-2}	282^{+5}_{-7}	$0.04^{+0.02}_{-0.01}$	$0.03^{+0.01}_{-0.01}$	$0.029^{+0.007}_{-0.002}$	$0.048^{+0.003}_{-0.007}$	$-5.453^{+0.005}_{-0.010}$	$-5.483^{+0.01}_{-0.007}$	TW (4 γ)
$14.5^{+0.3}_{-0.3}$	$-1.9^{+1.4}_{-0.9}$	287^{+3}_{-9}	$0.060^{+0.009}_{-0.024}$	$0.035^{+0.007}_{-0.016}$	$0.040^{+0.003}_{-0.004}$	—	$-5.469^{+0.007}_{-0.005}$	—	TW (2 γ)
$15.7^{+1.4}_{-1.3}$	13^{+9}_{-7}	276 ± 11	—	—	—	—	-5.458 ± 0.007	-5.487 ± 0.009	SI10
$14.1^{+1.5}_{-1.3}$	$3.3^{+2.5}_{-4.4}$	$290.5^{+9.8}_{-9.2}$	—	—	$0.0335^{+0.0063}_{-0.0045}$	$0.0476^{+0.0062}_{-0.0069}$	—	—	TR10
$13.9^{+0.03}_{-0.03}$	5^{+6}_{-5}	$278.2^{+13.8}_{-13.4}$	—	—	—	—	$-5.4599^{+0.0037}_{-0.0036}$	—	MI10
13.4 ± 1.5	—	$251.2^{+7.9}_{-10.8}$	—	—	—	—	$-5.4887^{+0.0013}_{-0.0018}$	—	PO08

8 ANALYSIS OF THE (O – C) TRANSIT TIMING DIAGRAM

In the first step, we analyse whether or not a quadratic departure from a linear fit is present in the transit timings. This could result from the direct interaction with a perturber on an extended orbit (Borkovits et al. 2011), or from the light travel timing produced by the motion of the star also induced by a hypothetical distant companion (Montalto 2010). This test can be performed following the approach of Pringle (1975) which measures the improvement of a fit by a quadratic parabola with respect to a simpler one by a straight line. However, the quadratic coefficient obtained by least squares is already zero within the error bars ($-0.9 \pm 3.5 \times 10^{-9}$ d). We thus conclude that there is no significant long-term quadratic trend in the data.

Then, we follow the analysis of Maciejewski et al. (2010). We compute a Lomb–Scargle periodogram on the transit timing variation (TTV) signal in order to detect a periodic oscillation that would reflect the perturbation of a close-in undetected body in the system. For that purpose, we use the generalized version (GLS) of the Lomb–Scargle periodogram (Zechmeister & Kürster 2009). Basically, the GLS fits a sinusoid to the data for each frequency by using the least-squares method, as the Lomb–Scargle algorithm, but in addition to that it allows for the presence of an additional constant term. False-alarm probabilities (FAP) are estimated by computing GLS periodograms on a large number of sets of artificial observations in which, for each epoch where a transit has been observed, we replace the measured (O – C) by a random value normally distributed around zero with a standard deviation equal to the uncertainty of that point. The number of periodograms containing a peak with a power above a given threshold out of the total number of trials represents our estimation of the FAP for that given threshold.

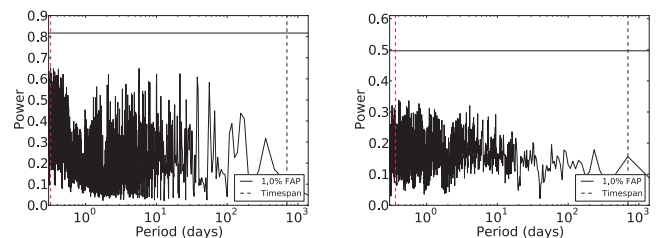
Fig. 5(a) shows the GLS periodogram obtained when considering only the transits used by Maciejewski et al. (2010, fig. 3). We obtain a dominant peak at a frequency $f_{\text{TTV}} = 0.0145$ cycle P^{-1} , which corresponds to $P_{\text{TTV}} = 127$ d and a power of 0.61, as shown by the arrow, in complete agreement with the result of Maciejewski et al. (2010). Nevertheless, the FAP associated with that power is 27 per cent. There is thus more than one chance out of four for this peak to be fortuitous. For the sake of completeness, the FAP thresholds of 0.1, 10^{-2} and 10^{-3} are represented by three horizontal lines in the two panels of Fig. 5. We did again the same analysis with all the data of Table 4. The results are displayed in Fig. 5(b). In that case, the peak with the highest power is now at $f_{\text{TTV}} = 0.0201$ cycle P^{-1} with an FAP of 56 per cent. It thus seems that the TTV signal does not contain any significant periodic oscillations.

**Figure 5.** Periodograms of the TTV signal. (a) Considering only the data used in Maciejewski et al. (2010). (b) Using all the data present in Table 4. The horizontal lines (from bottom to top) give the FAP thresholds of 0.1, 10^{-2} and 10^{-3} .

9 ANALYSIS OF THE (O – C) RADIAL VELOCITY DIAGRAM

We initially checked for the presence of either a linear or a quadratic term in the (O – C) radial velocity residuals by using the Pringle (1975) test. We considered the 2 γ solution and obtained that in both cases the coefficients are consistent with zero (0.00001 ± 0.00012 for the quadratic term and -0.030 ± 0.035 for the linear term).

A GLS periodogram was then computed. We considered initially the case of the residuals obtained fitting the 4 γ solution (Section 7). As seen in Fig. 6, no significant peaks can be found in the periodogram. The highest peak is at 0.35 d and has an FAP of 31 per cent. Alternatively, considering the residuals obtained by the 2 γ solution, we obtained the highest peak at 0.36 d with an FAP of 39 per cent. The FAP of the peaks are estimated with a bootstrapping method in the same way as in the previous section. The only difference is that the artificial data are made by shuffling (with repetition) the residuals instead of drawing random values from a normal distribution.

**Figure 6.** Periodogram of the radial velocity residuals considering the 4 γ solution (left) and the 2 γ solution (right). The continuous line denotes the 1 per cent FAP, while the dashed line denotes the time span of the observations.

10 DISCUSSION

Since the TTV signal does not present any long-term variations, or short period oscillations, one cannot assert that the system actually contains an additional planet. And, if such a companion does exist, its orbital parameters and mass are poorly constrained due to the lack of expected patterns in the current available data. Nevertheless, the residuals of the fit are quite large ($\sqrt{\chi_r^2} \simeq 2.30$ and $\sqrt{\chi_r^2} \simeq 1.5$ for transit and RV, respectively). As noticed also by other investigators in the past, these values do not indicate a satisfactory fit to the (O – C). The model is thus not complete. Several causes can be at the origin of this result among which we consider here stellar activity, the presence of an additional planet or exomoon and underestimated timing uncertainties.

10.1 Stellar activity

A possible source of TTVs can be the activity of WASP-3. Indeed, the existence of spots on the surface of the star, partially covered by the planet during transits, should produce fluctuations in the luminosity leading to some errors in the determination of the times of transit minimum (e.g. Sanchis-Ojeda et al. 2011; Oshagh et al. 2012). Moreover, the spots, if they exist, should not be the same between the beginning and the end of the observations given the long time span that has been covered (~ 4.5 yr). This would explain why no periodic oscillation is detected. Tripathi et al. (2010) reported fractional transit depth variations of the order of 7 per cent, even if the same authors were not confident whether these variations were genuine or due to systematics in their data. In addition, they report a mean $\log R'_{\text{HK}} = -4.9$ from their Keck spectra taken in 2008–2009.

On the other hand, we reanalysed the spectra taken with SOPHIE. From the 2007 observations (Pollacco et al. 2008) we derived a $\log R'_{\text{HK}}$ value of -4.95 , whereas the 2009–2010 observations (Simpson et al. 2010) provided a higher value for the activity index of $\log R'_{\text{HK}} = -4.80$ (Boisse et al. 2010). Therefore, it appears that the mean activity level of the star changed during these years approaching an active phase in 2010. Once considering also the upper limit on the stellar age and the rotation period reported by Miller et al. (2010, age < 2 Gyr and $P_{\text{rot}} = 4.3$ d), the presence of active regions on this star may not appear a rare circumstance. Despite no clear evidence of starspot crossing having been reported yet, this analysis clearly suggests a more intensive monitoring of the activity level of WASP-3 in order to understand its impact on photometric and radial velocity measurements.

10.2 Additional planet

We now give some constraints on the mass of a hypothetical planetary perturber. For that, we use both the dispersion of the O – C radial velocity and photometric diagrams. Concerning the radial velocity residuals, we adopted here the results coming from the 2γ solution, since no significant difference was found adopting instead the 4γ solution.

10.2.1 Radial velocities

In the literature, two main approaches are used to find the detection limits in radial velocity data. One is based on the χ^2 - and F -tests (e.g. Lagrange et al. 2009; Sozzetti et al. 2009) and another is based on a periodogram analysis (Cumming, Marcy & Butler 1999; Endl et al. 2001; Cumming 2004; Narayan, Cumming & Lin 2005). Here, the second approach was chosen due to the number

of measurements which is considered high enough for a reliable periodogram analysis.

For each period, a fake eccentric planetary signal is inserted in the data, while the original data are treated as random noise. On these new RV series, the power (in the periodogram) is calculated. The semiamplitude of the fake signal is changed until the FAP level is reached for all eccentricities e , times of periastron T_c and longitudes of periastron ϖ . In this paper, an FAP of 1 per cent, determined with 1000 shuffled time series, is used. Fake signals are tested for periods P between 1 and 20 d. The orbital elements of the eccentric signals range, in 10 steps, as follows: $0 \leq e \leq 1$, $0 \leq T_c \leq P$ and $0 \leq \varpi \leq 2\pi$. The final semiamplitude can be transformed in planetary mass and expresses the lower limit for detectable planets at that period with these data:

$$M_p \sin i = 1.2 \times 10^{-3} K \sqrt{1 - e^2} \left(\frac{P M_*^2}{2\pi G} \right)^{1/3}, \quad (8)$$

with the planetary mass in Earth masses, the semiamplitude K in m s^{-1} , the period P in days, the stellar mass M_* in solar masses and the gravitational constant G in $\text{m}^3 \text{kg}^{-1} \text{s}^{-2}$. Therefore, the continuous grey line in Fig. 7 denotes the limit in the perturber mass beyond which a signal would have been detected in the radial velocity data with a confidence limit equal to 99 per cent. The dashed lines show the 1σ uncertainty range of the radial velocity detection limit.

10.2.2 Photometry

We exclude compact systems which lead to unstable evolutions. Only circular and coplanar systems have been considered since they provide the strongest constraints and because the projected spin-orbit angle measure on WASP-3b by the RM effect is compatible with zero as demonstrated above, suggesting that if a planetary companion exists, the system is likely coplanar.

The radial velocity measurements are used to exclude any perturbers that would induce RV signal with an amplitude larger than the 1 per cent FAP threshold. The same exercise has been performed with the O – C of the transit timing measurements. For that, we simulated a large number of O – C on a grid of parameters of the perturber. We considered 400 periods P_{pert} ranging between 1.5 and 10 P_{transit} (where $P_{\text{transit}} = P$ is the period of the transiting planet), and 100 masses M_{pert} evenly distributed in logarithm between 0.01 and 5 M_J . For each period and mass, 60 simulations are performed with different initial longitudes between 0° and 360° . Among the 60 simulations, the one giving the periodogram with the lowest maximum amplitude is kept. If this amplitude is above the 1 per cent FAP threshold determined in Section 8, then the corresponding perturber should have been detected in the periodogram of the O – C (see Fig. 5), otherwise the perturber can exist but it is not detectable.

Fig. 7 (left) shows the results. The hatched region, which extends up to a period ratio of 1.5, delineates the chaotic orbits which are excluded. The boundary of this region has been derived from the stability criterion of Gladman (1993). The grey curve fixes the limit of the perturber's mass from the radial velocity measurements. Any perturber in the grey region would induce a periodic RV signal with a significant amplitude. And finally, the black regions delineate the perturbers that produce TTVs with significant oscillating terms. Combining all the information, it turns out that the radial velocity technique excludes any perturber as massive as Jupiter up to a period ratio of 10, and the TTV measurements provide stronger constraints close to mean motion resonances.

In the second step, we focused on perturbers that do not produce any significant periodic RV signals or periodic TTV signals.

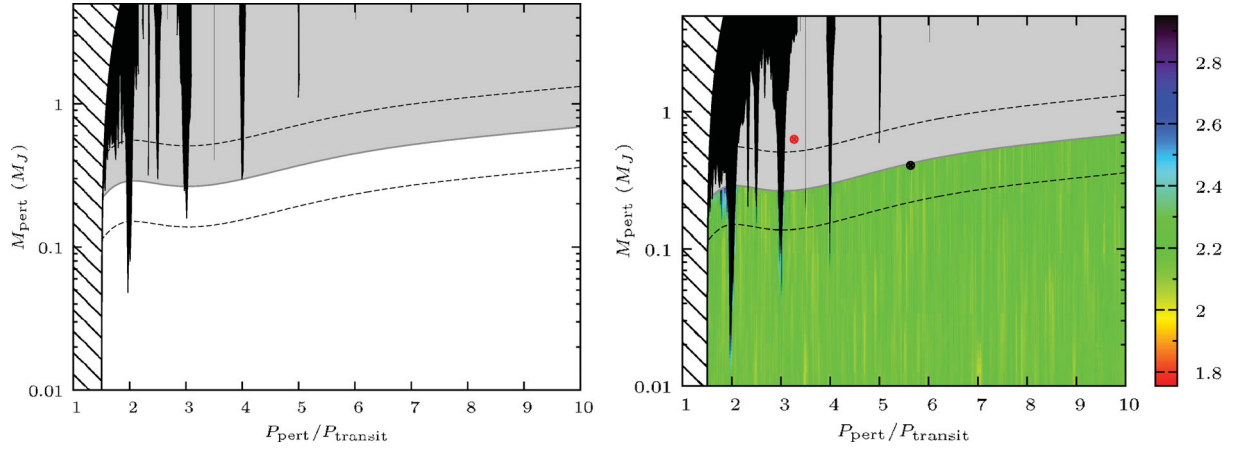


Figure 7. Left: constraints on the maximal mass of a perturber: 99 per cent confidence detection limits from periodograms of transit timing (black) and radial velocity data (grey). The dashed lines denote the uncertainty range of the radial velocity detection region. The hatched lines indicate unstable orbits. Right: reduced $\sqrt{\chi_r^2}$ values resulting from the fit of the observed O – C timing residuals with our model. The calculation is extended over the radial velocity undetectability region, but we also show the regions that produce a 3σ in black. Note that these regions overlap with the transit timing detectability regions of the left-hand panel.

Such perturbers are located in the white region of Fig. 7 (left). For those perturbers, we check whether they can reproduce the O – C transit timing diagram or not. For that purpose, we use the same grid of parameters as in Fig. 7 (left), and for each set of initial conditions, we compute the expected TTVs and the reduced χ^2 with respect to the observations. The results are displayed in Fig. 7 (right). The hatched and the grey regions are the same as in Fig. 7 (left). The black regions correspond now to simulated TTVs above the 3σ level. This threshold is obtained from the χ^2 distribution with 33 degrees of freedom. It corresponds to $\chi_r^2 = \chi_{r,\min}^2(1 + 1.821)$ or $\sqrt{\chi_r^2} = 2.95$. The colour scale represents the $\sqrt{\chi_r^2}$ from the lowest values in red up to the 3σ threshold in dark violet. The red circle shows the best fit to the observation with $\sqrt{\chi_r^2} = 1.76$. However, such a perturber with a mass of $0.63 M_J$ should have been detected in the radial velocity analysis. The best fit within the undetectable perturbers is just below the RV detection threshold with $M_{\text{pert}} = 0.41 M_J$ and $P_{\text{pert}} = 5.63 P_{\text{transit}}$, but the corresponding reduced χ^2 is only $\sqrt{\chi_r^2} = 1.83$. The improvement is very weak. Moreover, from Fig. 7 (right), one can see that such values of the reduced χ^2 are spread more or less randomly within the undetectable region.

As noted by Maciejewski et al. (2010), the presence of an outer companion less massive than WASP-3b but still on a short period orbit would make the system quite unusual. Multiplanetary systems containing at least a Jupiter-mass planet are indeed much wider, and the less massive planet is usually the closest to the star (e.g. Lissauer et al. 2011).

10.3 Exomoon

An exomoon is also supposed to generate a periodic oscillation in the TTV. However, Maciejewski et al. (2010) have already discarded this hypothesis since the transits do not show any duration variations shifted in phase by $\pi/2$ with respect to the timing variations. Here, we perform a more detailed analysis based on the results of Kipping (2009).

First of all, we check that an exomoon can have a stable orbit. If the moon is less than twice as dense as the planet, the minimum distance of the moon is set by the Roche limit. Let ξ be the semimajor axis of a hypothetical satellite divided by the Hill radius, i.e. $a_s =$

ξR_H , where a_s is the semimajor axis of the moon and R_H is the Hill radius. According to Kipping (2009), ξ should satisfy the following inequality:

$$\chi_{\min} \lesssim \xi \lesssim \frac{1}{3}, \quad (9)$$

where $\xi_{\min} = 1/186 \times (M_s/M_{\oplus})^{-0.063} (P/1 \text{ d})^{-2/3}$ represents the Roche limit. In this expression, M_s is the mass of the satellite and P is the orbital period of the planet. For an exomoon of the mass of the Earth’s Moon, we get $\xi_{\min} = 0.0047$, and for an exomoon of the mass of the Earth, $\xi_{\min} = 0.0036$. In both cases, χ_{\min} is lower than $1/3$. For moons whose density is more than twice that of the planet, the Roche limit would be inside the planet; therefore, the minimum distance would correspond to the planetary radius and the above inequality would be automatically satisfied. Therefore, an exomoon can exist on a stable orbit around WASP-3.

Then, we estimate the maximal rms amplitude (δ_{TTV}) of TTV that an exomoon on a coplanar circular orbit can produce. According to Kipping (2009), this amplitude is given by

$$\delta_{\text{TTV}} = \frac{1}{\sqrt{2}} \frac{P}{2\pi} \left(\frac{M_{\text{ps}}}{3M_{\star}} \right)^{1/3} \mu(1 - \mu)^{1/3} \xi, \quad (10)$$

with $\mu = M_s/M_{\text{ps}}$ and M_{ps} is the sum of the planet mass and the satellite mass. Without any constraint on μ , the maximum of the product $\mu(1 - \mu)^{1/3}$ is attained for $\mu = 3/4$, and is equal to $3/4^{1/3}$. However, by definition, the Moon should have a lower mass than the planet. If the transit light curves are those of the planet, μ should be lower than $1/2$, and probably much lower. Let us assume that $\mu = 1/2$; this will provide the upper limit of δ_{TTV} . If the planet has an exomoon, the Keplerian orbit derived in the previous section is that of the planet–satellite barycentre around the star. Thus, the fitted mass corresponds to M_{sp} . Using $M_{\text{sp}}/M_{\star} = 1.5 \times 10^{-3}$, one obtains

$$\delta_{\text{TTV}} \leq \frac{1}{\sqrt{2}} \frac{1}{2^{4/3}} \frac{P}{2\pi} \left(\frac{M_{\text{sp}}}{3M_{\star}} \right)^{1/3} \xi = 9.4 \xi \quad [\text{min}]. \quad (11)$$

For $\xi = \xi_{\max} = 1/3$, this leads to $\delta_{\text{TTV}} \leq 3.1 \text{ min}$. The result is larger than the observed rms of the O – C which is equal to 1.1 min. Thus, a ‘satellite’ as massive as the planet ($\mu = 1/2$) is able to produce significant TTV with an amplitude comparable to the observed one.

We now assume that the observed O – C is only due to a hypothetical satellite. Expecting that this satellite should have a much

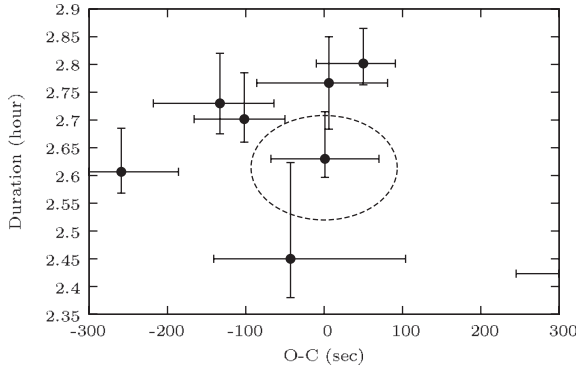


Figure 8. Transit durations against O – C transit timing residuals for the new transits presented in this work. Overplotted is a representative signal produced by an exomoon having $M_s = 0.35M_J$ and period $\chi = 1/3$.

smaller mass than the planet, we derive its mass for $\xi = \xi_{\max} = 1/3$ such that $\delta_{\text{TTV}} = 1.1$ min. One gets $\mu = 0.14$, which corresponds to a mass ratio of $M_s/M_p = 0.17$, or $M_s \approx 0.35M_J$. Thus, the lowest mass satellite, on a circular orbit, that can account for the observed rms of the O – C is still large. Assuming the same density as a giant planet like Jupiter, the radius of this satellite should be $0.46R_J$. Such a big satellite, if it existed, would produce detectable transits in the light curve. We also noticed that a search for additional transiting objects in the NASA *EPOXI* mission WASP-3 light curve resulted in a null detection (Ballard et al. 2011). However, we note that according to Domingos, Winter & Yokoyama (2006) the value of the critical semimajor axis could approach the value of 0.9309 in units of the Hill radius, for retrograde moons. In this case, we can obtain a more stringent constraint on the maximum mass of the moon which could be equal to $M_s/M_p = 0.04$ or $M_s \approx 0.07M_J$. In Fig. 8, we also show our transit durations against the O – C residuals. In the case of an exomoon being responsible for the claimed TTVs, we should expect the observations to trace an ellipse in this diagram since the TTVs and the transit duration variations (TDVs) produced by an exomoon are shifted in phase by $\pi/2$ (Kipping 2009). For illustration, we overplot the expected signal that the above-mentioned prograde satellite ($M_s = 0.35M_J$ and $\chi = 1/3$) should generate. Evidently, given the large error bars of our measurements it is not possible to explore this possibility, and additional more accurate measurements are required for this analysis.

10.4 Underestimated uncertainties

It is difficult to ascertain up to which level different instruments, observing conditions, reduction and transit fitting procedures may affect the results reported in Table 4. To address this point, it would be necessary to homogeneously reduce and analyse all the data collected so far by all the different groups, an approach which is not easy to put into practice. In principle, all the transits considered here were presented in referred journals and this ensures that accurate procedures like those reported here have been applied to estimate transit timing errors. It is our opinion however that error underestimation cannot be completely ruled out. New observations will be certainly welcome to clarify this problem.

11 CONCLUSIONS

In this work, we provided a thorough analysis on the presence of additional bodies in the WASP-3 system. This analysis serves to

Table 7. An example of the material available as Supporting Information with the online version of the paper (the light curves). The following data are from the light curve of 2009 May 15.

BJD _{TDB} – 245 0000	Flux	e_{Flux}	Airmass
4967.428677015	1.00462	0.00297	2.01600
4967.429880762	1.00018	0.00234	1.99700
4967.431130812	1.00254	0.00322	1.97800
4967.432346160	0.99567	0.00282	1.96000
...

improve our understanding of close-in Jupiters and in particular to clarify if these planets are indeed isolated or not.

In addition to the present eight new transits of WASP-3b acquired at the Crow Observatory–Portalegre in Portugal, we reanalyse all the photometric and radial velocity measurements acquired so far for this system. We conclude that there is no convincing evidence of additional planetary companions in this system; both the transit timing and the radial velocity residuals do not present significant periodicities (FAP of 56 and 31 per cent for the transit and radial velocity in the best case scenario, respectively) or long-term trends.

Combining all transit timing and radial velocity information, we obtained that any perturber more massive than $M \gtrsim 100M_{\oplus}$ and with period up to 10 times the period of the inner planets is excluded at 99 per cent confidence limit.

We also investigated the possible presence of an exomoon on this system and determined that considering the scatter of the O – C transit timing residuals a coplanar exomoon would likely produce detectable transits; a hypothesis that can be ruled out by observations conducted by other researchers. In the case where the orbit of the moon is not coplanar, the current accuracy of transit timing and transit duration measurements prevents us from making any significant statement. For retrograde moons, the maximum mass allowed at the critical semimajor axis is around $0.1M_J$.

Finally, on the basis of our reanalysis of SOPHIE data we noted that WASP-3 passed from a less active ($\log R'_{\text{HK}} = -4.95$) to a more active ($\log R'_{\text{HK}} = -4.8$) state between 2007 and 2010. Despite the fact that no clear spot crossing has been reported for this system so far, we therefore pointed out the need for a more intensive monitoring of the activity level of this star in order to understand its impact on photometric and radial velocity measurements.

Our light curves are made available as Supporting Information with the online version of the article. Table 7 presents an example of the online material for the light curve of 2009 May 15.

ACKNOWLEDGMENTS

This work was supported by the European Research Council/European Community under the FP7 through Starting Grant agreement number 239953, and through grant reference PTDC/CTE-AST/098528/2008 from Fundação para a Ciência e a Tecnologia (FCT, Portugal). MM, NCS and SS also acknowledge the support from FCT through programme Ciência 2007 funded by FCT/MCTES (Portugal) and POPH/FSE (EC) and in the form of fellowship references SFRH/BPD/71230/2010 and SFRH/BPD/47611/2008. GB thanks Paris Observatory and CAUP for providing the necessary computational resources for this work. We thank the referee, Dr David Kipping, whose valuable comments helped us to improve this manuscript.

NOTE ADDED IN PROOF

We note that recently Nascimbeni et al. (2012) reported an independent analysis of the WASP-3 system, presenting also novel photometric data. We did not include these data in our work; nevertheless, the conclusions reached by those authors appear similar to ours.

REFERENCES

- Ballard S. et al., 2011, *ApJ*, 732, 41
 Boisse I. et al., 2010, *A&A*, 523, 88
 Borkovits T., Csizmadia Sz., Forgács-Dajka E., Hegedüs T., 2011, *A&A*, 528, 53
 Charbonneau D., Brown T. M., Latham D. W., Mayor M., 2000, *ApJ*, 529, 45
 Chatterjee S., Ford E. B., Matsumura S., Rasio F. A., 2008, *ApJ*, 686, 580
 Christiansen J. L. et al., 2011, *ApJ*, 726, 94
 Claret A., Bloemen S., 2011, *A&A*, 529, 75
 Cumming A., 2004, *MNRAS*, 354, 1165
 Cumming A., Marcy G. W., Butler R. P., 1999, *ApJ*, 526, 890
 Domingos R. C., Winter O. C., Yokoyama T., 2006, *MNRAS*, 373, 1227
 Eastman J., Siverd R., Gaudi B. S., 2010, *PASP*, 122, 935
 Endl M., Kürster M., Els S., Hatzes A. P., Cochran W. D., 2001, *A&A*, 374, 675
 Fabrycky D., Tremaine S., 2007, *ApJ*, 669, 1298
 Gazak J. Z., Johnson J. A., Tonry J., Dragomir D., Eastman J., Mann A. W., Agol E., 2012, *Adv. Astron.*, 2012, 30
 Gelman A., Rubin D., 1992, *Stat. Sci.*, 7, 457
 Gibson N. P. et al., 2008, *A&A*, 492, 603
 Gladman B., 1993, *Icarus*, 106, 247
 Goldreich P., Tremaine S., 1980, *ApJ*, 241, 425
 Hirano T., Suto Y., Taruya A., Narita N., Sato B., Johnson J. A., Winn J. N., 2010, *ApJ*, 709, 458
 Jurić M., Tremaine S., 2008, *ApJ*, 686, 603
 Kipping D. M., 2009, *MNRAS*, 392, 181
 Kozai Y., 1962, *AJ*, 67, 591
 Kurucz R. L., 1993, in Dworetzky M. M., Castelli F., Faraggiana R., eds, *ASP Conf. Ser. Vol. 44, Peculiar versus Normal Phenomena in A-type and Related Stars*. Astron. Soc. Pac., San Francisco, p. 87
 Lagrange A.-M., Desort M., Galland F., Udry S., Mayor M., 2009, *A&A*, 495, 335
 Lissauer J. J. et al., 2011, *ApJS*, 197, 8
 Littlefield C., 2011, preprint (arXiv:1106.4312L)
 Maciejewski G. et al., 2010, *MNRAS*, 407, 2625
 McLaughlin D. B., 1924, *ApJ*, 60, 22
 Mandel K., Agol E., 2002, *ApJ*, 580, 171
 Mayor M., Queloz D., 1995, *Nat*, 378, 355
 Miller G. R. M. et al., 2010, *A&A*, 523, 52
 Montalto M., 2010, *A&A*, 521, 60
 Nagasawa M., Ida S., Bessho T., 2008, *ApJ*, 678, 498
 Narayan R., Cumming A., Lin D. N. C., 2005, *ApJ*, 620, 1002
 Nascimbeni V. et al., 2012, *A&A*, in press (arXiv:1210.3045)
 Nelson R. P., Papaloizou J. C. B., Masset F., Kley W., 2000, *MNRAS*, 318, 18
 Oshagh M., Boué G., Haghighipour N., Montalto M., Figueira P., Santos N. C., 2012, *A&A*, 540, 62
 Pál A., 2008, *MNRAS*, 390, 281
 Pál A., 2012, *MNRAS*, 420, 1630
 Pollacco D. et al., 2008, *MNRAS*, 385, 1576
 Pont F., Zucker S., Queloz D., 2006, *MNRAS*, 373, 231
 Press W. H., Teukolsky S. A., Vetterling W. T., Flannery B. P., 1992, *Numerical recipes in FORTRAN. The art of scientific computing*, 2nd edn. Cambridge Univ. Press, Cambridge
 Pringle J. E., 1975, *MNRAS*, 170, 633
 Rossiter R. A., 1924, *ApJ*, 60, 15
 Sada P. V. et al., 2012, *PASP*, 124, 212
 Sanchis-Ojeda R., Winn J. N., Holman M. J., Carter J. A., Osip D. J., Fuentes C. I., 2011, *ApJ*, 733, 127
 Santos N. C., Israelian G., Mayor M., 2004, *A&A*, 415, 1153
 Simpson E. K. et al., 2010, *MNRAS*, 405, 1867
 Sneden C., 1973, *ApJ*, 184, 839
 Sousa S., Santos N. C., Israelian G., Mayor M., Monteiro M. J. P. F. G., 2007, *A&A*, 469, 783
 Sousa S., Alapini A., Israelian G., Santos N. C., 2010, *A&A*, 512, 13
 Sozzetti A., Torres G., Charbonneau D., Latham D. W., Holman M. J., Winn J. N., Laird J. B., O'Donovan F. T., 2007, *ApJ*, 664, 1190
 Sozzetti A., Torres G., Latham D. W., Stefanik R. P., Korzennik S. G., Boss A. P., Carney B. W., Laird J. B., 2009, *ApJ*, 697, 544
 Stetson P. B., 1987, *PASP*, 99, 191
 Stetson P. B., 1994, *PASP*, 106, 250
 Szabó Gy. M., Szatmáry K., Divéki Zs., Simon A., 2006, *A&A*, 450, 395
 Triard A. H. M. J. et al., 2010, *A&A*, 524, 25
 Tripathi A., Winn J. N., Johnson J. A., 2010, *ApJ*, 715, 421
 Vogt S. S. et al., 1994, in Crawford D. L., Craine E. R., eds, *Proc. SPIE Vol. 2198, Instrumentation in Astronomy VIII*. SPIE, Bellingham, p. 362
 Weidenschilling S. J., Marzari F., 1996, *Nat*, 384, 619
 Wu Y., Murray N., 2003, *ApJ*, 589, 605
 Zechmeister M., Kürster M., 2009, *A&A*, 496, 577

APPENDIX A: THE NORMALIZED PLANET DISTANCE

Here we derive the expression for the normalized planet distance z presented in equation (1). Assuming a circular orbit and a constant projected velocity (v) of the transiting planet on the plane of the sky, at any given instant t during the transit the normalized distance z can be written as

$$z^2 = \left(\frac{b}{R_*}\right)^2 + \left(v \frac{t - T_0}{R_*}\right)^2,$$

where b is the impact parameter, R_* is the radius of the star and T_0 is the time of transit minimum. At the time of the first or the fourth contact, we have

$$z^2 = (r + 1)^2 = \left(\frac{b}{R_*}\right)^2 + \left(v \frac{T_d}{2R_*}\right)^2,$$

where r is the ratio of the radius of the planet to the radius of the star and T_d is the total transit duration (from the first to the fourth contact). Assuming the projected velocity during the transit to be identical to the orbital velocity, we can write

$$v = \sqrt{\frac{GM_*}{a}},$$

where G is the gravitational constant, M_* is the mass of the star, a is the semimajor axis and we neglected the mass of the planet. Eliminating in the first equation above the impact parameter derived from the second, using the third Kepler law and introducing the definition of the mean stellar density

$$\rho_* = \frac{M_*}{(4/3)\pi R_*^3},$$

we obtain equation (1):

$$z^2(t) = \left(\frac{8\pi^2 G}{3P}\right)^{2/3} \rho_*^{2/3} \left[(t - T_0)^2 - \left(\frac{T_d}{2}\right)^2 \right] + (1 + r)^2.$$

APPENDIX B: RM EFFECT DURING THE INGRESS AND THE EGRESS

In this appendix, we introduce a new analytic representation of the RM effect valid during the ingress and the egress of the transit, that

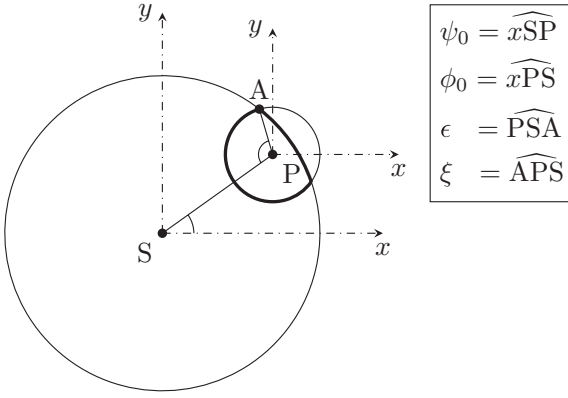


Figure B1. Definition of the ψ_0 , ϕ_0 , ϵ and ξ angles introduced in the text.

is between the first and the second contact and between the third and the fourth contact. During these phases, the formula presented by Hirano et al. (2010) accounts for the velocity of the star below the disc of the planet considering the value of the velocity at the centre of the disc of the planet, and it is therefore valid for the small planets approximation. We instead integrated the velocity profile below the disc and calculated the average velocity which makes our approach consistent with the calculation of Hirano et al. (2010) for the remaining phases of the transit. This derivation is based on the method described in Pál (2012).

Therefore, if we define X and Y as the coordinates of the centre of the planet at a given instant during the transit, according to the choice of parameters we adopted in this paper, we have

$$X = \frac{(1 - e \sin \omega)}{\sqrt{1 - e^2}} \left(\frac{8\pi^2 G}{3P} \right)^{1/3} \rho_\star^{1/3} (t - T_0),$$

$$Y = \frac{(1 - e \sin \omega)}{\sqrt{1 - e^2}} \sqrt{(1 + r)^2 - \left(\frac{8\pi^2 G}{3P} \right)^{2/3} \rho_\star^{2/3} \left(\frac{T_d}{2} \right)^2}.$$

Then if λ is the spin–orbit angle projected on the plane of the sky, in the rotated coordinate system whose vertical axis is aligned with the projected spin axis of the star, the coordinates x and y are given by

$$x = X \cos \lambda - Y \sin \lambda,$$

$$y = X \sin \lambda + Y \cos \lambda.$$

Let ψ_0 , ϕ_0 , ϵ and ξ be defined as in Fig. B1 with respect to the xy rotated coordinate system, then

$$\psi_0 = \arctan_2(y, x),$$

$$\phi_0 = \psi_0 + \pi.$$

Assuming that the radius of the star is normalized to unity, one gets

$$\epsilon = a \cos \left(\frac{1 - r^2 + z^2}{2z} \right),$$

$$\xi = a \cos \left(\frac{r^2 + z^2 - 1}{2rz} \right),$$

where

$$z = \sqrt{x^2 + y^2}.$$

Defining now the angles ψ_a , ψ_b , ϕ_a and ϕ_b as

$$\psi_a = \psi_0 - \epsilon,$$

$$\psi_b = \psi_0 + \epsilon,$$

$$\phi_a = \phi_0 - \xi,$$

$$\phi_b = \phi_0 + \xi,$$

and defining the following functions:

$$A(\alpha, \beta, \gamma) = \frac{1}{2} \alpha^2 \beta \sin \gamma + \frac{1}{2} \alpha \beta^2 \left(\gamma + \frac{1}{2} \sin 2\gamma \right) + \frac{1}{2} \beta^3 \left(\gamma + \frac{1}{3} \sin^3 2\gamma \right),$$

$$B(\alpha, \beta, \gamma) = \frac{1}{2} \alpha \beta \sin \gamma + \frac{1}{2} \beta^2 \left(\gamma + \frac{1}{2} \sin 2\gamma \right),$$

the subplanet velocity v_p is given by

$$\frac{v_p}{v \sin i} = \frac{A_{\text{tot}}}{B_{\text{tot}}}, \quad (\text{B1})$$

where

$$A_{\text{tot}} = A(0, 1, \psi_b) - A(0, 1, \psi_a) + A(x, r, \phi_b) - A(x, r, \phi_a),$$

$$B_{\text{tot}} = B(0, 1, \psi_b) - B(0, 1, \psi_a) + B(x, r, \phi_b) - B(x, r, \phi_a).$$

During the full transit phase, equation (10) reduces to

$$\frac{v_p}{v \sin i} = x, \quad (\text{B2})$$

which is equal to equation (A8) of Hirano et al. (2010).

SUPPORTING INFORMATION

Additional Supporting Information may be found in the online version of this article:

Light curves. Data files for the light curves of 2009 May 15, and 2011 April 13, April 26, June 2, July 20, August 13, August 26 and September 8.

Please note: Wiley–Blackwell are not responsible for the content or functionality of any supporting materials supplied by the authors. Any queries (other than missing material) should be directed to the corresponding author for the article.

This paper has been typeset from a \LaTeX file prepared by the author.